Chinese Chemical Letters 35 (2024) 109580

Contents lists available at ScienceDirect

Chinese Chemical Letters

journal homepage: www.elsevier.com/locate/cclet

Efficient photocatalytic biomass-alcohol conversion with simultaneous hydrogen evolution over ultrathin 2D NiS/Ni-CdS photocatalyst

Zongyi Huang[b,1], Cheng Guo[a,1], Quanxing Zheng[c], Hongliang Lu[c], Pengfei Ma[c], Zhengzhong Fang[c], Pengfei Sun[b], Xiaodong Yi[b,*], Zhou Chen[a,*]

[a] College of Materials, Key Laboratory of High Performance Ceramic Fibers (Xiamen University), Ministry of Education, Xiamen University, Xiamen 361005, China
[b] State Key Laboratory of Physical Chemistry of Solid Surfaces, College of Chemistry and Chemical Engineering, Xiamen University, Xiamen 361005, China
[c] Technology Center, China Tobacco Fujian Industrial Co., Ltd., Xiamen 361021 China

ARTICLE INFO

Article history:
Received 14 November 2023
Revised 24 January 2024
Accepted 25 January 2024
Available online 2 February 2024

Keywords:
Photocatalysis
Biomass-alcohol oxidation
H_2 evolution
Dual-functional catalysis

ABSTRACT

The photocatalytic conversion of biomass into high-value chemicals, coupled with simultaneous hydrogen (H_2) evolution, leveraging the electrons and holes generated by solar energy, holds great promise for addressing energy demands. In this study, we constructed a dual functional photocatalytic system formed by NiS loaded on Ni doped two-dimensional (2D) CdS nanosheet (NiS/Ni-CdSNS) heterostructure for visible-light-driven H_2 evolution and ethanol oxidation to acetaldehyde. Remarkably, the 2D NiS/Ni-CdSNS exhibited significant activity and selectivity in both photocatalytic H_2 evolution and ethanol oxidation, achieving yields of 7.98 mmol g^{-1} h^{-1} for H_2 and 7.33 mmol g^{-1} h^{-1} for acetaldehyde. The heterogeneous interface of the composite facilitated efficient charge separation, while NiS provided abundant sites for proton reduction, thereby promoting the overall dual-functional photocatalytic activity. Density functional theory calculations further reveal that both Ni doping and NiS loading can reduce the reaction energy barrier of ethanol oxidation of free radicals, and NiS/Ni-CdSNS composite materials exhibit stronger ethanol C-H activation ability to generate key intermediate $^{\bullet}CH(OH)CH_3$ on the surface. This work serves as a valuable guide for the rational design of efficient dual functional photocatalytic systems that combine H_2 evolution with the selective conversion of organic compounds into high-value chemicals.

Amidst the global challenges of fossil energy scarcity, environmental pollution, and greenhouse effect, the utilization of biomass energy has emerged as a vital strategy in alleviating the ecological pressures caused by human social development [1–3]. However, the conventional utilization of biomass primarily focus on heat generation, which unfortunately results in the emission of environmentally harmful substances [4]. Recently, transforming biomass into high-value chemicals has been a growing emphasis [5–8]. Although microorganisms or enzymes show potential to convert biomass into biogas, the long conversion cycle hinders its effectiveness in industrial production [8,9]. In contrast, the photocatalytic biomass conversion into high-value chemicals and green hydrogen (H_2) presents a promising avenue for sustainable development, which utilizes the highly active photogenerated carriers, distinguishing it from the traditional organic biomass synthesis conducted under high temperature or pressure conditions [10,11]. Overall, this unique mechanism holds great potential for efficient and sustainable energy conversion.

Selective oxidation of biomass alcohols to carbonyl compounds, particularly aldehydes, is a significant focus in biomass activation research [12,13]. Aldehydes play a vital role in organic synthesis and diverse applications in the production of chemicals [14,15]. Conventional methods of acetaldehyde production through ethylene oxidation have drawbacks such as high energy requirements and environmental pollution [16]. In contrast, the photocatalytic oxidation of ethanol, the most common alcohol in biomass, to acetaldehyde offers a more environmentally friendly alternative [17,18]. Additionally, the photocatalytic process activates the C–H bonds of alcohols, allowing for the generation of clean H_2 fuel [19–22]. This innovative approach combines alcohol oxidation promoting the production of green hydrogen fuel using renewable biomass in the current low-carbon era [11,23]. However, challenges remain in achieving highly selective alcohol oxidation and facilitating H_2 evolution in aqueous solution without the use of expensive and harmful organic solvents. Therefore, the development of

* Corresponding authors.
E-mail addresses: xdyi@xmu.edu.cn (X. Yi), zhouchen@xmu.edu.cn (Z. Chen).
[1] These authors contributed equally to this work.

https://doi.org/10.1016/j.cclet.2024.109580
1001-8417/

an efficient dual-functional photocatalyst is crucial for effectively enabling the oxidation of ethanol into acetaldehyde while simultaneously promoting H_2 evolution in environmentally friendly aqueous conditions.

Many semiconductor-based materials, including transition metal chalcogenides, have been used for solar-driven energy conversion [24–27]. CdS is a particularly promising material due to its moderate band levels [28]. Moreover, when CdS reaches the two-dimensional (2D) scale, it also has a larger specific surface area and more active sites like other traditional 2D materials, allowing for carries rapidly transfer to surface and participation in reactions [29,30]. Thus, 2D CdS nanosheets (CdSNS) emerges as an ideal material for photocatalytic reaction. However, the rapid recombination of photogenerated carries hinders the photocatalytic activity of single phase 2D CdSNS [31–33]. To overcome this limitation, incorporating cocatalysts or rational composite materials has proven to be one of the most effective methods, which can enhance the efficiency of carrier separation and facilitate redox reactions [34–38]. For example, Yang *et al.* employed a mixed heterojunctions integrated CdS nanorods with WS_2 nanosheets to promote the transport of charge carriers, enhancing the hydrogen evolution activity [39]. These strategies are crucial in facilitating the separation and transfer of charges, as well as improving the stability of photocatalysts. Nickel, an electron-enriched cocatalyst, is an ideal choice due to its non-toxicity, low cost, and has been widely used in various photocatalytic reactions [40,41]. Inspired by these advantages, doping Ni into the synthesis of CdSNS can optimize the band structure of CdSNS by changing the amount of Ni incorporation and form NiS co-catalyst *in situ* on the surface of CdSNS together, which can therefore promote the oxidation of ethanol to acetaldehyde and the evolution rate of H_2.

In this work, we present a promised approach to synthesize NiS/Ni-CdSNS composed of NiS loaded on Ni doped CdS ultrathin nanosheets composites through a one-pot method. This strategic assembly results in the development of an efficient dual-functional photocatalytic system capable of selectively oxidizing ethanol into acetaldehyde while simultaneously promoting H_2 evolution. The introduction of Ni and NiS into the CdSNS photocatalyst optimizes its band structure, leading to enhanced light absorption and improved separation of photogenerated charge carrier. Consequently, the photocatalytic efficiency of the NiS/Ni-CdSNS is significantly higher than that of pure CdSNS. Mechanistic studies and density functional theory calculations reveal that the key intermediate $^{\bullet}CH(OH)CH_3$ originated from the C−H activation of ethanol in the formation of acetaldehyde has the optimal reaction energy barrier on NiS/Ni-CdSNS. This work provides a potential design protocol for achieving dual-functional photocatalysis, enabling the selective oxidation of organic alcohols into valuable chemical feedstocks while facilitating H_2 evolution.

The synthetic process of 2D NiS/Ni-CdSNS composites photocatalyst is illustrated in Fig. 1a. Briefly, the CdSNS and various CdSNS with different mass ratios of Ni were synthesized by a simple one-pot solvothermal method. As witnessed by the scanning electron microscope (SEM) image and transmission electron microscope (TEM) in Figs. 1b, e, and Fig. S1 (Supporting information). The pure CdSNS consists of numerous ultrathin 2D nanosheets. Upon adding Ni into the CdSNS, the resulting Ni doped CdSNS nanohybrids also retain the sheet-like structure of pure CdSNS without any observable aggregation (Figs. 1c, d, f, g, and Fig. S2 in Supporting information). As shown high-resolution TEM (HRTEM) imaging in Fig. S1d, the lattice spacing of 0.36 nm corresponds to the (100) plan of CdSNS. Meanwhile, in the 5 wt% Ni doped CdSNS nanohybrids, two distinct sets of lattice stripes are visible, with 0.36 nm and 0.27 nm representing the (100) crystal plane of CdSNS and (300) crystal plane of NiS (Fig. 1h), respectively. Moreover, the actual mass ratios of Ni in different samples were quantitatively determined utilizing energy dispersive X-ray (EDX) analysis and the results were displayed in Table S1 (Supporting information). It can be seen from Table S1 that the mass ratio of Ni for CdSNS increase linearly with increased feed ratio and the actual ratio is similar to the feed ratio.

Nevertheless, to further explore the composition of the samples formed by Ni incorporating with CdSNS, HRTEM was further employed on samples with different ratios of Ni. Fig. S3 (Supporting information) concluded that at low Ni doping levels, Ni elements are uniformly doped into CdSNS to form Ni-CdSNS. As the amount of Ni incorporated into CdSNS increases, NiS crystal phases appear, forming binary NiS/Ni-CdSNS consisted with coexistence of Ni doping and NiS loading. Furthermore, the corresponding selected area electron diffraction (SAED) pattern in Fig. 1i displays two sets of diffraction fringes, proving further evidence for the formation of heterojunctions between NiS and Ni-CdSNS. Additionally, EDX element mappings spectroscopy confirms the presence of homogeneous Ni signal within the NiS/Ni-CdSNS composite (Fig. 1j). X-ray diffraction (XRD) pattern was employed to investigate the crystal structures of the CdSNS, Ni-CdSNS, and NiS/Ni-CdSNS nanohybrids. The XRD patterns in Fig. S4 (Supporting information) revels diffraction peaks at 24.6°, 26.5°, and 51.8°, which correspond to the ultrathin 2D CdSNS and are well-matched to the crystal structure of cubic CdS (JCPDS No. 41–1049) [42]. Meanwhile, the diffraction peak at 32.2°, 35.7°, and 48.8° can be indexed to (300), (021), and (131) lattice planes of NiS, respectively, corresponding to the crystal structure of rhombohedral NiS (JCPDS No. 12–0041). In the XRD patterns of the different Ni-CdSNS and NiS/Ni-CdSNS samples with varying mass ratios of Ni, all the observed diffraction peaks are consistent with the XRD peaks of pure CdSNS. However, due to the relatively low content, poor crystallinity, and high dispersion of NiS within the nanohybrid samples, no distinct diffraction peak corresponding to NiS is detected. This further confirms that NiS loading and Ni doping does not alter the morphology and crystalline phase of cubic CdSNS, which is consistent with the SEM and TEM results described earlier. As shown in Fig. S5 (Supporting information), the N_2 isotherm adsorption/desorption curve over a series of samples was depicted. This result demonstrated that the incorporating of Ni did not have a significant impact on the specific surface area of CdSNS.

To investigate the surface chemical state of the samples in depth, X-ray photoelectron spectroscopy (XPS) was conducted. The survey spectra in Fig. S6a (Supporting information) show clear signals of Cd and S elements for both samples, while the Ni element is detected only in the 5NiS/Ni-CdSNS sample (Figs. S6b-d and Table S2 in Supporting information). The Cd 3d spectra of CdSNS exhibit two peaks at 403.7 and 410.4 eV, corresponding to Cd $3d_{5/2}$ and Cd $3d_{3/2}$, respectively [43]. The pure CdSNS sample shows two peaks in the S 2p spectrum at approximately 161.2 and 160.0 eV, assigned to S $2p_{1/2}$ and S $2p_{3/2}$, respectively. These binding energies are in consistent with those of S^{2-} species [44]. In the Ni 2p spectrum of 5NiS/Ni-CdSNS, two characteristic peaks at 872.6 and 855.0 eV can be observed, corresponding to the Ni $2p_{1/2}$ and $2p_{3/2}$ spectrum of Ni^{2+} [41,45]. A slight Cd 3d shift towards higher binding energies by 0.9 eV is observed in 5NiS/Ni-CdSNS then CdSNS. Similarly, the relevant binding energies of S 2p in the 5NiS/Ni-CdSNS composite show a slight positive shift then that of CdSNS. These results indicate electron transfer from CdSNS to NiS and Ni in the 5NiS/Ni-CdSNS composite. The observed shifts in the peaks further suggest electronic interactions and charge transfer within the composite material. The optical properties and band gaps of the as-prepared photocatalysts were analyzed using UV–vis diffuse reflectance spectra (DRS) and XPS valence band spectrum (VB-XPS). Based on these characterizations (Fig. S7 in Supporting information), the band structure of the nanohybrid shows that the

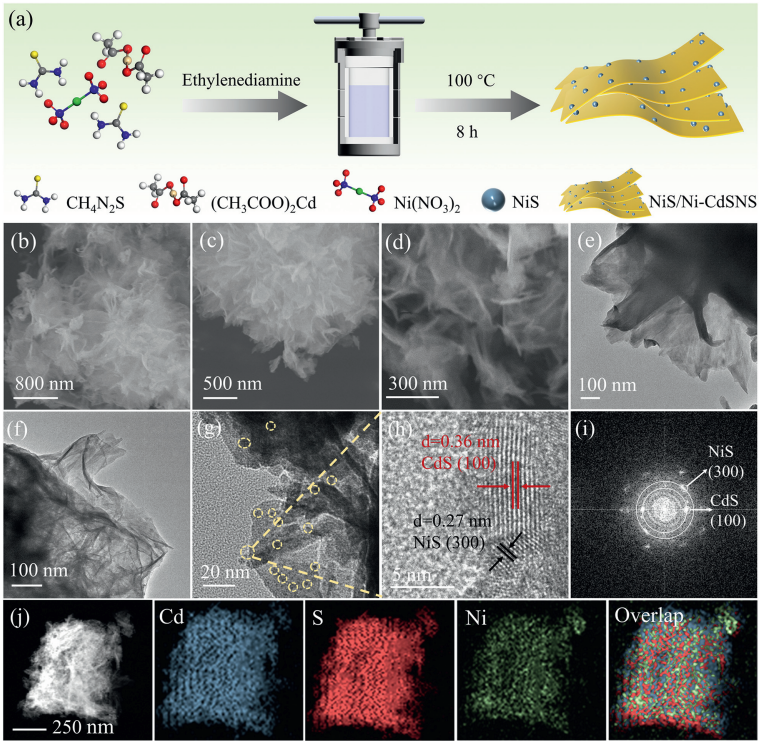

Fig. 1. (a) Schematic diagram for the synthesis of 2D NiS/Ni-CdSNS. SEM images of (b) CdSNS and (c, d) 5NiS/Ni-CdSNS. TEM images of (e) CdSNS and (f, g) 5NiS/Ni-CdSNS. (h) HRTEM image and (i) selected area electron diffraction pattern of 5NiS/Ni-CdSNS. (j) Corresponding EDX elemental mapping images of the 5NiS/Ni-CdSNS sample.

photogenerated electrons in the E_{CB} have a sufficiently negative potential to reduce protons, while the holes in the E_{VB} can oxidize ethanol to acetaldehyde. This suggests that the NiS/Ni-CdSNS exhibits favorable band positions for efficient photocatalytic reactions.

To evaluate the photocatalytic performance of catalysts, the dehydrogenation and oxidation activity of ethanol was evaluated and quantified by gas chromatography (Figs. S8 and S9 in Supporting information). Fig. 2a and Fig. S10 (Supporting information) illustrates that, comparing CdSNS with Ni-CdSNS and NiS/Ni-CdSNS composites. CdSNS demonstrates a relative low formation rate for H_2 (0.57 mmol g^{-1} h^{-1}) and acetaldehyde (0.31 mmol g^{-1} h^{-1}). Upon Ni doping, both formation rate of H_2 and acetaldehyde exhibit significant enhancement. It is observed that the 5NiS/Ni-CdSNS achieves the optimal photocatalytic rate, with the formation rates of H_2 and acetaldehyde reaching 7.98 and 7.33 mmol g^{-1} h^{-1}, respectively, which are approximately 14 times higher than those achieved by pure CdSNS. Meanwhile, regarding the by-products of the ethanol photocatalytic oxidation reaction, the formation rate of 2,3-butanediol remains consistently low. However, the generation rate of acetaldehyde decreases when the doping amount of Ni exceeds 5 wt%. This can be ascribed to the excessive coverage of

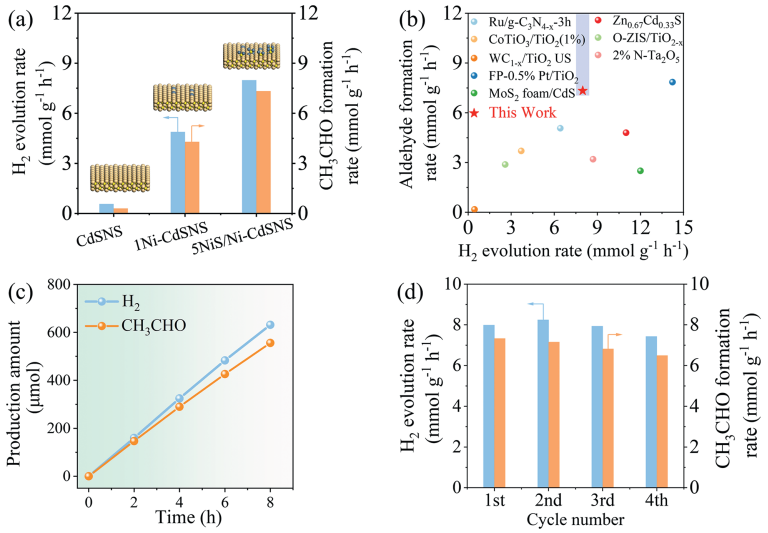

Fig. 2. (a) Photocatalytic performance of H_2 evolution integrated with selective ethanol oxidation. (b) Comparison of synergistic H_2 evolution and alcohols oxidation by photocatalytic method (Table S2 in Supporting information for details). (c) Generation of H_2 and acetaldehyde photocatalyzed by 5NiS/Ni-CdSNS as a function of reaction time. (d) Stability tests over 5NiS/Ni-CdSNS.

NiS on the surface of CdSNS blocks the active sites for ethanol oxidation. Interestingly, when Ni doping and NiS loading coexist in binary NiS/Ni-CdSNS, the selectivity of acetaldehyde can be significantly enhanced (Fig. S11 in Supporting information). We speculate that the Ni doping and NiS loading can alter the charge distribution on the surface of CdSNS, with electrons transferring from CdS to Ni and NiS, enhancing the adsorption strength of ethanol on the CdSNS surface, and promoting the deep oxidation of ethanol to acetaldehyde. This indicates that Ni and NiS has an important impact on the selectivity of oxidation products. When comparing the photocatalytic performance of NiS/Ni-CdSNS with other that photocatalytic alcohol oxidation reactions, it stands among the leading performances (Fig. 2b and Table S3 in Supporting information). Furthermore, 5NiS/Ni-CdSNS further was applied to other biomass-alcohols (Fig. S12 in Supporting information), which indicates that the 5NiS/Ni-CdSNS has good application prospects for the biomass alcohols oxidation. A time-dependent analysis of the 5NiS/Ni-CdSNS was conducted to investigate the kinetics of acetaldehyde evolution and ethanol consumption (Fig. 2c). The results indicate that the production of acetaldehyde increases progressively with the increase in H_2 concentration. Over 8 h of reaction time, the amount of H_2 and acetaldehyde can reach up to 632 and 556 μmol, respectively. In addition, the generation of deep oxidation products acetic acid and CO_2 was not observed in long-term kinetic testing (Fig. S13 in Supporting information), indicating that the product acetaldehyde can exist stably in the reaction system.

Moreover, comparing the photocatalytic performance of ethanol oxidation with the specific surface areas of each catalyst itself, it was found that binary 5NiS/Ni-CdSNS still has the highest normalized reaction efficiency (Table S4 in Supporting information). The catalytic stability of 5NiS/Ni-CdSNS was assessed through four cycle stability tests, and the results (Fig. 2d) demonstrate the catalytic performance remains nearly unchanged throughout the cycles. This further confirms the good stability of the NiS/Ni-CdSNS composites in the dual-function system. Additionally, the XRD, SEM, TEM, and XPS reveal that no significant changes in the structures, morphology, and chemical state of the composite before and after the photocatalytic reaction (Figs. S14-S16 in Supporting information). This suggests the structural integrity and stability of the 5NiS/Ni-CdSNS nanohybrid throughout the photocatalytic process.

Furthermore, the charge-transfer dynamics of the composite materials were assessed through photoelectrochemical characterizations. As shown in Fig. 3a, it can be seen that all the composite exhibits a significantly enhanced current density compared to pure CdSNS (1.1 μA/cm), with 5NiS/Ni-CdSNS showing the highest current density (5.3 μA/cm). This indicates that compared to pure CdSNS and Ni-CdSNS, binary NiS/Ni-CdSNS has the highest photocurrent density. The electrochemical impedance spectra (EIS) analysis in Fig. 3b reveals that 5NiS/Ni-CdSNS exhibits a smaller semicircle radius in the Nyquist plot compared to other samples. This indicates that 5NiS/Ni-CdSNS possesses the smallest resistance and highest transmission efficiency. Furthermore, linear sweep voltammetry (LSV) suggests 5NiS/Ni-CdSNS exhibits significantly enhanced current density (Fig. S17 in Supporting information), indicating that Ni doping and NiS loading jointly promote the charge transfer and separation ability of 2D 5NiS/Ni-CdSNS. To further elucidate the mechanism behind the enhanced charge transfer dynamics of the 2D photocatalyst materials, steady-state photoluminescence (PL) spectra and time-resolved PL (TRPL) were conducted. In Fig. S18 (Supporting information), the PL signal of 5NiS/Ni-CdSNS composite was weaker than that of Ni-CdSNS and CdSNS. This indicates that Ni doping and NiS loading coexist can significantly promote the separation of electron hole pairs and slow down the recombination probability [46,47]. To further quantitatively analyze the photogenerated electron transfer dynamics, TRPL was performed as shown in Fig. 3c. Compared to pure CdSNS with an average PL lifetime (τ_{avg}) of 5.3 ns, the 5NiS/Ni-CdSNS exhibits an extended τ_{avg} of 6.5 ns. The significant increase in τ_{avg} indicates faster electron transfer and reduced electro-hole recombination in 5NiS/Ni-CdSNS. This further confirms the efficient separation of photogenerated electron–hole pairs between Ni, NiS, and CdSNS in the composites. In summary, the steady-state PL spectra and TRPL characterization reveal that the NiS/Ni-CdSNS composites leads to PL quenching and a shortened average PL lifetime. To further understand the underlying mechanisms, the spin resonance (ESR) on the NiS/Ni-CdSNS and CdSNS were conducted in Fig. S19 (Supporting information). The ESR spectrum of the NiS/Ni-CdSNS sample reveals a strong signal peak at 3370 G, indicating the presence of S vacancies, which is crucial for efficient charge transfer and improved photocatalytic properties [48,49]. These findings provide further evidence to support the enhanced photocatalytic performance of NiS/Ni-CdSNS and highlight the role of S vacancies in facilitating the charge separation process.

The charge transfer path between Cd, S, and Ni at the NiS/Ni-CdSNS is crucial for understanding the photocatalytic mechanism. To investigate this, the photo-assisted *in-situ* XPS was carried out to observe the transfer process of photogenerated charge on the surface of NiS/Ni-CdSNS during light irradiation. The results showed that the binding energy of Cd 3d and S 2p in NiS/Ni-CdSNS shows a slight increase after illumination (Figs. 3d and e). On the other hand, the peaks of Ni 2p shifted to a negative binding energy under *in-situ* irradiation, indicating that NiS acts as an electron acceptor under light irradiation (Fig. 3f). This suggests that the photogenerated electrons flow from Ni-CdSNS to NiS under light irradiation, while the holes accumulate in Ni-CdSNS. These findings provide direct evidence for the carrier transfer pathway and matches the above discussions.

The effect of charge carriers and free radical intermediates on NiS/Ni-CdSNS was investigated by incorporating corresponding scavengers (Fig. 4a). It is observed that in the absence of light and catalyst, no detectable amount of acetaldehyde and H_2 are produced. This suggests light and catalyst are essential for ethanol conversion. When ethanol was removed, H_2 production is almost negligible, indicating that the H_2 is derived from ethanol and integrated into the synthesis of acetaldehyde. Then, when the reaction takes place in an oxygen (electrons sacrificial agents) environment, the production of H_2 is markedly reduced, whereas the generation rates of acetaldehyde increase from 7.3 mmol g^{-1} h^{-1} to 11.9 mmol g^{-1} h^{-1}. This suggests that the consumption of electron enhances the ability of the holes to oxidize ethanol. Conversely, the addition of EDTA-2Na (holes sacrificial agents) significantly hinders the conversion rate of ethanol. These results lead to the inference that both photogenerated electrons and holes are involved in the coupled H_2 evolution reaction during the oxidation of ethanol to acetaldehyde.

In situ ESR spectrum was further used for capturing the free radical intermediates generated in the photocatalytic oxidation of ethanol. The ESR spectrum show in Fig. 4b depict characteristic sextet signal peaks for both the CdSNS and 5NiS/Ni-CdSNS composite. These peaks can be attributed to the hydroxyethyl radical ($^{\bullet}CH(OH)CH_3$) radical, which is generated by the activation of ethanol $C_{\alpha}-H$ bond. The $^{\bullet}CH(OH)CH_3$ radical cannot be detected under dark conditions. Importantly, the ESR signal intensity of the 5NiS/CdSNS is stronger than that of CdSNS, indicating a higher concentration of $^{\bullet}CH(OH)CH_3$ produced by the 5NiS/Ni-CdSNS. Hence, it can be concluded that photogenerated holes selectively activate the C—H bond of ethanol, facilitating the generation of the $^{\bullet}CH(OH)CH_3$ radical. Overall, these results suggest that the NiS/Ni-CdSNS is involved in a coupled H_2 evolution reaction during the oxidation of ethanol to acetaldehyde.

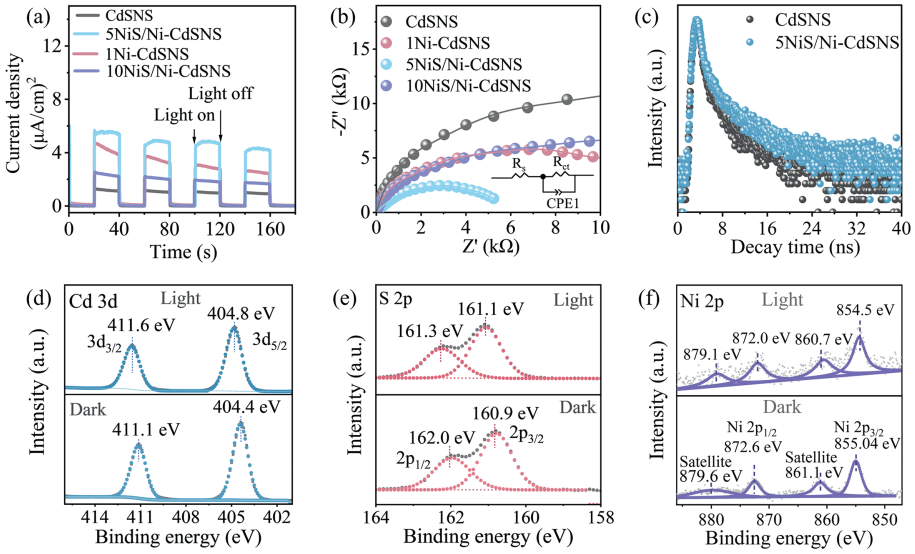

Fig. 3. (a) Transient photocurrent and (b) electrochemical impedance spectroscopy (EIS) spectra of CdSNS and obtained composites. (c) Time-resolved PL spectra of CdSNS and 5NiS/Ni-CdSNS composite. *In situ* XPS spectra of (d) Cd 3d, (e) S 2p, and (f) Ni 2p for the 5NiS/Ni-CdSNS.

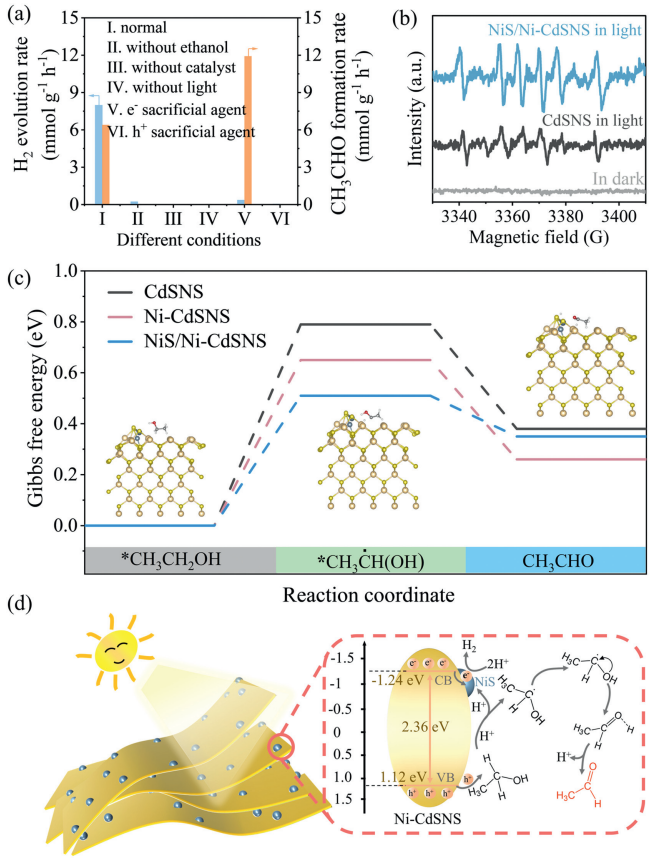

Fig. 4. (a) The photocatalytic performance of H_2 evolution integrated with ethanol oxidation under different conditions. (b) ESR spectra of CdSNS and NiS/Ni-CdSNS with the addition of DMPO. (c) Calculated energy profile for ethanol oxidative dehydrogenation and acetaldehyde production on CdSNS, Ni-CdSNS, and NiS/Ni-CdSNS. The reaction structure diagram in the figure shows the reaction structure diagram of ethanol on the NiS/Ni-CdSNS surface. (d) Schematic diagram of photocatalytic H_2 evolution integrated with acetaldehyde synthesis.

To further investigate the influence of the dual cocatalyst, density function theory (DFT) was used to analysis the ethanol oxidation process and the reaction energy barriers on the CdSNS, Ni-CdSNS, and NiS/Ni-CdSNS surface. The results, as shown in Fig. 4c, Fig. S20 and Table S5 (Supporting information), indicate that the Gibbs free energy changes of the key intermediate $^{\bullet}CH(OH)CH_3$ formed from ethanol are 0.79, 0.65, and 0.51 eV on CdSNS, Ni-CdSNS, and NiS/Ni-CdSNS surface models, respectively. This suggests the surface of NiS/Ni-CdSNS is most favorable for the production of $^{\bullet}CH(OH)CH_3$, which is consistent with the ESR radical capture experiment. Furthermore, the Gibbs energy changes from the continuous oxidation of $^{\bullet}CH(OH)CH_3$ to acetaldehyde were 0.41, 0.39, and 0.16 eV over CdSNS, Ni-CdSNS, and NiS/Ni-CdSNS surface models, respectively. In both reaction steps, the NiS/Ni-CdSNS sample consistently exhibits the lowest Gibbs free energy change value. This indicates the reaction energy barrier for the ethanol oxidation to acetaldehyde on NiS/Ni-CdSNS is the lowest, confirming the experimental conclusion mentioned above.

Based on the above results, a plausible reaction mechanism for the oxidation ethanol into acetaldehyde and H_2 evolution was proposed in Fig. 4d. Under light irradiation, photogenerated electrons and holes are simultaneously generated in 5NiS/Ni-CdSNS. The Ni and NiS acts as a promoter for accelerating charges separation by capturing the photogenerated electrons. Furthermore, due to the ultrathin nanosheet morphology of 5NiS/Ni-CdSNS, the photogenerated charge carriers can effectively migrate to the surface of the photocatalyst. Then, the generation of $^{\bullet}CH(OH)CH_3$ intermediates and protons can generate from $C_{\alpha}-H$ activization of ethanol by photogenerated holes in the VB of Ni-CdSNS. Subsequently, $^{\bullet}CH(OH)CH_3$ adsorbed on the surface of Ni-CdSNS undergoes further oxidation, resulting in the formation of acetaldehyde. At the same time, the photogenerated electrons at the NiS sites reduce the proton derived from the C−H bond of ethanol, producing H_2. Overall, the proposed mechanism suggests that the simultaneous generation of photogenerated electrons and holes, facilitates efficient charge separation, promotes the activation of the $C_{\alpha}-H$ bond in ethanol, and enables the oxidation of intermediates to acetaldehyde.

In this study, a NiS/Ni-CdSNS composite was synthesized using one-pot solvothermal method, showing efficient dual-functional photocatalytic properties for converting ethanol into acetaldehyde and H_2 evolution. Ni doping and NiS loading improved the band

structure, enhancing light absorption and carrier separation, resulting in increased photocatalytic efficiency compared to pure CdSNS. The reaction rates of acetaldehyde and H_2 in 5NiS/Ni-CdSNS were 14 times higher than in pure CdSNS, with acetaldehyde selectivity increasing from 40% to 91%. Mechanism studies revealed a crucial role for $^{\bullet}CH(OH)CH_3$ radical in acetaldehyde formation, with the lowest energy barrier observed in NiS/Ni-CdSNS. This study introduces a new approach for dual-functional photocatalysis, enabling selective oxidation of organic alcohols into valuable chemical feedstocks while producing H_2.

Declaration of competing interest

The authors declare that they have no known competing financial interests or personal relationships that could have appeared to influence the work reported in this paper.

Acknowledgments

This work was supported by the National Key R&D Program of China (No. 2022YFB1903200), the National Natural Science Foundation of China (Nos. U23A2087, 22372137, 22102136, 22072057, 22227802, 22172126), the Key Research and Development Program of Guangxi (No. GUIKE AB23026116), the Fundamental Research Funds for the Central Universities (Nos. 20720220105, 20720232005), and the XMU Training Program of Innovation and Enterpreneurship for Undergraduates (Nos. 2022Y1132, 202310384027).

Supplementary materials

Supplementary material associated with this article can be found, in the online version, at doi:10.1016/j.cclet.2024.109580.

References

[1] M.Y. Qi, M. Conte, M. Anpo, et al., Chem. Rev. 121 (2021) 13051–13085.
[2] N. Luo, T. Montini, J. Zhang, et al., Nat. Energy 4 (2019) 575–584.
[3] S. Song, J. Qu, P. Han, et al., Nat. Commun. 11 (2020) 4899.
[4] J. Radonić, N. Jovčić Gavanski, M. Ilić, et al., Stoch. Env. Res. Risk A 31 (2017) 2201–2213.
[5] J.C. Colmenares, R. Luque, Chem. Soc. Rev. 43 (2014) 765–778.
[6] L. Yuan, Y.H. Li, Z.R. Tang, et al., J. Catal. 390 (2020) 244–250.
[7] Z. Chen, S. Li, Q. Mo, et al., Chin. Chem. Lett. 34 (2023) 108196.
[8] Z.M.A. Bundhoo, R. Mohee, Ultrason. Sonochem. 40 (2018) 298–313.
[9] J.Y. Huang, Z.Y. Huang, S. Xu, et al., Energy Technol 10 (2022) 2200362.
[10] X. He, N. Zheng, R. Hu, et al., Adv. Funct. Mater. 31 (2021) 2006505.
[11] M.Y. Qi, Y.H. Li, M. Anpo, et al., ACS Catal. 10 (2020) 14327–14335.
[12] Q. Yang, T. Wang, Z. Zheng, et al., Appl. Catal. B: Environ. 315 (2022) 121575.
[13] F.S. Xing, R.Y. Zeng, C.C. Cheng, et al., Appl. Catal. B: Environ. 306 (2022) 121087.
[14] C. Bianchini, P.K. Shen, Chem. Rev. 109 (2009) 4183–4206.
[15] Z. Guo, B. Liu, Q. Zhang, et al., Chem. Soc. Rev. 43 (2014) 3480–3524.
[16] L. Chen, J. Tang, L.N. Song, et al., Appl. Catal. B: Environ. 242 (2019) 379–388.
[17] J.J. Murcia, M.C. Hidalgo, J.A. Navío, et al., Catal. Today 196 (2012) 101–109.
[18] R. Wang, J. Zhang, Y. Zhu, et al., ACS Appl. Mater. Inter. 14 (2022) 2848–2859.
[19] M. Torras, P. Molet, L. Soler, et al., Adv. Energy Mater. 12 (2022) 2103733.
[20] N. Luo, T. Hou, S. Liu, et al., ACS Catal. 10 (2020) 762–769.
[21] C.L. Tan, M.Y. Qi, Z.R. Tang, Y.J. Xu, Appl. Catal. B: Environ. 298 (2021) 120541.
[22] C. Wang, B. Weng, Y. Liao, et al., Chem. Commun. 58 (2022) 10691–10694.
[23] Y. Zhang, Z. Liu, C. Guo, et al., Appl. Surf. Sci. 571 (2022) 151284.
[24] L. Yuan, M.Y. Qi, Z.R. Tang, Y.J. Xu, Angew. Chem. Int. Ed. 60 (2021) 21150–21172.
[25] J.Y. Huang, Z.Y. Huang, S. Xu, et al., Energy Technol. 10 (2022) 2200362.
[26] X.Y. Lian, J.G. Zhang, Y. Zhan, et al., J. Hazard. Mater. 406 (2020) 124705.
[27] D. Zhang, P. Wang, F. Chen, et al., Chin. Chem. Lett. 31 (2020) 2795–2798.
[28] X.Y. Lian, Z.Y. Huang, Y.Q. Zhang, et al., Chemosphere 313 (2023) 137351.
[29] X. Yang, W. Liu, C. Han, et al., Mater. Today Phys. 15 (2020) 100261.
[30] Y. Zhang, T.R. Chang, B. Zhou, et al., Nat. Nanotechnol. 9 (2014) 111–115.
[31] S. Cheng, Q. Xiong, C. Zhao, X. Yang, Chinese J. Struc. Chem. 41 (2022) 58–64.
[32] Z.Y. Huang, Q.Y. Zhang, X.T. Ma, et al., Mater. Today Chem. 29 (2023) 101475.
[33] E.H. Zhang, Q.H. Zhu, J.H. Huang, et al., Appl. Catal. B: Environ. 293 (2021) 120213.
[34] P. Zhou, Q.H. Zhang, Y.G. Chao, et al., Chem 7 (2021) 1033–1049.
[35] J. Ran, M. Jaroniec, S.Z. Qiao, Adv. Mater. 30 (2018) 1704649.
[36] H. Yuan, W. Shi, J. Lu, et al., Chem. Eng. J. 454 (2023) 140442.
[37] X.P. Wang, Z.L. Jin, X. Li, Rare Metals 42 (2023) 1494–1507.
[38] B. He, C. Bie, X. Fei, et al., Appl. Catal. B: Environ. 288 (2021) 119994.
[39] Z. Cirena, Y. Nie, Y. Li, et al., Chin. Chem. Lett. 34 (2023) 107726.
[40] C. Ding, C. Zhao, S. Cheng, X. Yang, Chinese J. Catal. 43 (2022) 403–409.
[41] J.Y. Li, M.Y. Qi, Y.J. Xu, Chinese J. Catal. 43 (2022) 1084–1091.
[42] J. Zhang, L. Qi, J. Ran, et al., Adv. Energy Mater. 4 (2014) 1301925.
[43] D.R. Jones, R. Phillips, W.J.F. Gannon, et al., Sci. Rep. 9 (2019) 11573.
[44] T. Tian, X. Jin, N. Guo, et al., Appl. Catal. B: Environ. 308 (2022) 121227.
[45] R.J. Feng, K.W. Wan, X.Y. Sui, et al., Nano Today 37 (2021) 101080.
[46] Y. Wei, G. Cheng, J. Xiong, et al., J. Energy Chem. 32 (2019) 45–56.
[47] F. Zhao, H. Li, T. Liu, et al., Mol. Catal. 474 (2019) 110418.
[48] Y.W. Zhu, J. Chen, L.H. Shao, et al., Appl. Catal. B: Environ. 268 (2020) 1188744.
[49] J. He, L. Hu, C. Shao, et al., ACS Nano 15 (2021) 18006–18013.